

# ALMA: a mathematics-driven approach for determining tuning parameters in generalized LASSO problems, with applications to MRI

Gianluca Giacchi<sup>\*†‡§¶</sup>, Isidoros Iakovidis<sup>\*||</sup>, Matthias Stuber<sup>†</sup>, Micah M. Murray<sup>†§</sup>, Bastien Milani<sup>†¶</sup> and Benedetta Franceschiello<sup>‡§¶</sup>

<sup>\*</sup>Department of Mathematics, University of Bologna, Bologna, Italy

<sup>†</sup> Department of Diagnostic and Interventional Radiology, Lausanne University Hospital and University of Lausanne, Lausanne, Switzerland

<sup>‡</sup> Institute of Systems Engineering, School of Engineering, HES-SO Valais-Wallis, Sion, Switzerland

<sup>§</sup>The Sense Innovation and Research Center, Lausanne and Sion, Switzerland

<sup>||</sup>These authors provided equal first-authorship contribution

<sup>¶</sup>These authors provided equal last-authorship contribution

## Abstract

Magnetic Resonance Imaging (MRI) is a powerful technique employed for non-invasive in vivo visualization of internal structures. Sparsity is often deployed to accelerate the signal acquisition or overcome the presence of motion artifacts, improving the quality of image reconstruction. Image reconstruction algorithms use TV-regularized LASSO (Total Variation-regularized LASSO) to retrieve the missing information of undersampled signals, by cleaning the data of noise and while optimizing sparsity. A tuning parameter moderates the balance between these two aspects; its choice affecting the quality of the reconstructions. Currently, there is a lack of general deterministic techniques to choose these parameters, which are oftentimes manually selected and thus hinder the reliability of the reconstructions. Here, we present ALMA (Algorithm for Lagrange Multipliers Approximation), an iterative mathematics-inspired technique that computes tuning parameters for generalized LASSO problems during MRI reconstruction. We analyze quantitatively the performance of these parameters for imaging reconstructions via TV-LASSO in an MRI context on phantoms.

Although our study concentrates on TV-LASSO, the techniques developed here hold significant promise for a wide array of applications. ALMA is not only adaptable to more generalized LASSO problems but is also robust to accommodate other forms of regularization beyond total variation. Moreover, it extends effectively to handle non-Cartesian sampling trajectories, broadening its utility in complex data reconstruction scenarios. More generally, ALMA provides a powerful tool for numerically solving constrained optimization problems across various disciplines, offering a versatile and impactful solution for advanced computational challenges.

## Index Terms

Basis pursuit, compressed sensing, compressive sensing, convex analysis, convex optimization, denoising, inverse problems, LASSO, magnetic resonance, MRI, regression, sparsity, total variation

## I. INTRODUCTION

**M**AGNETIC Resonance Imaging (MRI) is a non-invasive radiation-free technique that has become widespread over the last forty years. MRI exploits the magnetization of protons in water molecules of tissues to provide 3D anatomical images. To reduce the acquisition time, the MR signal is sampled below its Nyquist frequency, and the missing information is retrieved by solving numerically the generalized (unconstrained) LASSO (g-LASSO), a convex optimization problem in the form:

$$\text{minimize} \quad \frac{1}{2} \|Ax - b\|_2^2 + \frac{\lambda}{2} \|\Phi x\|_1, \quad x \in \mathbb{C}^n, \quad (1)$$

where  $n$  is the dimensionality of the problem,  $A \in \mathbb{C}^{m \times n}$  is a *measurement operator*,  $b \in \mathbb{C}^m$  is the *measurement*,  $\Phi \in \mathbb{C}^{N \times n}$  is a *sparsity promoting transform*, and  $\|\cdot\|_p$  denotes the  $p$ -(quasi-)norm on  $\mathbb{C}^d$  ( $0 < p < \infty$ ):

$$\|y\|_p^p = \sum_{j=1}^d |\Re(y_j)|^p + |\Im(y_j)|^p, \quad y \in \mathbb{R}^d.$$

If  $\Phi$  is the  $n \times n$  identity matrix, g-LASSO is called LASSO. In the case of MRI, where the sampled signal is the Fourier transform of the proton density weighted by the effects of T1 and T2 time-relaxations, cf. [1],  $n$  is the number of voxels,  $x$  is an image,  $A = UFC$  encodes the undersampling operator  $U$ , the discrete Fourier transform (DFT)  $F$  and  $C$  is a complex

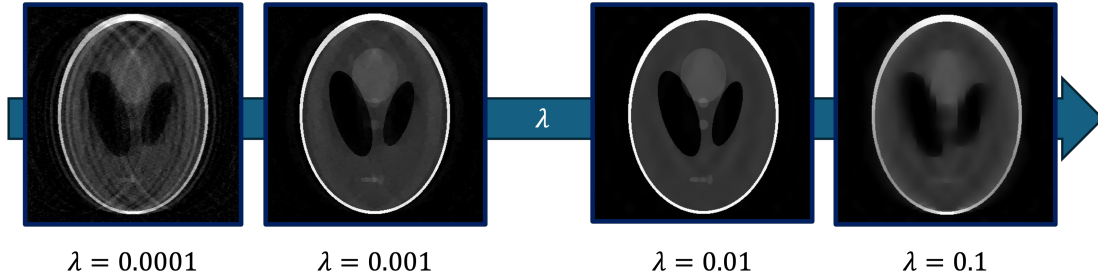


Fig. 1: Impact of tuning parameters. Small values of  $\lambda$  produce pronounced artifacts. Large values of  $\lambda$  produce oversmoothing.

matrix which encompasses the channel extension and the sensitivity mapping,  $b$  is the noisy undersampled measurement and  $\Phi$  can be the DFT, the discrete wavelet transform (DWT), the discrete cosine transform (DCT), or other sparsity promoting transforms, according to the situation, cf. [2]. The addendum  $\|Ax - b\|_2^2$  measures the fidelity of the reconstruction, quantifying the distance between the measured data  $b$  and the model  $Ax$ , whereas  $\|\Phi x\|_1$  measures the sparsity of  $\Phi x$ . The parameter  $\lambda > 0$  acts as a trade-off, balancing the two contributions, and it is called tuning parameter. For small values of  $\lambda$ , the addendum  $\lambda\|\Phi x\|_1$  becomes negligible and the image reconstructed via g-LASSO will be noisy and biased by the artifacts resulting from the missing information. On the contrary, large values of  $\lambda$  force  $\|\Phi x\|_1$  to be small, resulting in overly smoothed images with poor resolution (see fig. 1).

The choice of this tuning parameter highly affects the quality of the reconstructions. However, there remains no generally effective procedure to provide well-performing tuning parameters. Consequently, the tuning parameter is chosen manually or heuristically, without following standard protocols. An automatic procedure to detect optimal tuning parameters is therefore needed to heavily reduce the post-processing of MR acquired signals, to increase the reproducibility of MR reconstructions, and the adequacy of reconstructions, according to the specific clinical or research question at hand.

The mathematical motivation for considering g-LASSO problems relates to the constrained LASSO problem (or quadratically constrained basis pursuit):

$$\text{minimize} \quad \|x\|_1 \text{ subject to } x \in \mathbb{R}^n, \quad \|Ax - b\|_2 \leq \eta, \quad (2)$$

whose solution, if unique, is known to be  $m$ -sparse, where  $m$  is the rank of the measurement matrix  $A \in \mathbb{R}^{m \times n}$ , cf. [3]. Under these assumptions, there exists a parameter  $\lambda' \geq 0$ , related to the *Lagrange multipliers*, such that the unconstrained LASSO has an  $m$ -sparse solution. For simplicity, we refer to  $\lambda'$  as Lagrange multiplier. In broad terms, solving LASSO with tuning parameter  $\lambda'$  provides sparse solutions. The question thus arises whether Lagrange multipliers play an analogous role for generalized LASSO problems, where  $\Phi$  is a general sparsity promoting transform. To answer this question, we build an iterative algorithm, that we call ALMA (*Algorithm for Lagrange Multipliers Approximation*), to provide an *approximate Lagrange multipliers* (ALM) and reconstruct a MR image from undersampled data, artificially corrupted by Gaussian noise, according to the MRI sampling procedure, by solving g-LASSO with such obtained parameter. The quality of the reconstructions, along with the optimality of the tuning parameters, is measured by means of three metrics, quantifying the main aspects of an effective MRI reconstruction: the impact of noise and the impact of artifacts, see Section III-C below. The purpose of this study is three-fold:

- To define ALMA, an iterative procedure to compute ALMs, that can be easily generalized to more common versions of g-LASSO.
- To understand the efficiency of ALMs as tuning parameters for TV weighted g-LASSO in the context of MRI.
- To evaluate the quality of reconstructions by means of image quality metrics.

Our results provide new insights into the impact of theoretical mathematical analysis on MR image reconstructions, shifting the focus from guessing tuning parameters to obtaining concrete estimates of noise energy.

## II. THEORETICAL MODEL

### A. Mathematical rationale

The LASSO problem is fundamental in the recovery of sparse vectors. Its origins trace back to the seminal contributions of F. Santosa and W. W. Symes [4], S. Chen and D. Donoho [5], [6], and R. Tibshirani [7]. Notably, within the domain of MRI, M. Lustig and colleagues [2], [8], [9], [10], [11] pioneered the applications of both LASSO and g-LASSO. The purpose of this section is to motivate our conjecture that Lagrange multipliers could be used as effective tuning parameters for imaging reconstruction with g-LASSO. For the sake of completeness, we shall clarify the notion of sparsity comprehensively.

*Definition 1:* A vector  $x \in \mathbb{R}^n$  is  $m$ -sparse if  $\|x\|_0 = \#\{j : x_j \neq 0\} \leq m$ . When  $m$  is irrelevant for the understanding, we say that  $x$  is sparse.

In the definition above,  $\#A$  denotes the cardinality of the set  $A$ . A slightly modification of the proof [3, Theorem 3.1] yields to the following result:

*Theorem 1:* Let  $A \in \mathbb{R}^{m \times n}$  be a measurement matrix and  $\eta \geq 0$ . If the minimizer  $x^\#$  of the constrained LASSO:

$$\text{minimize} \quad \|x\|_1 \text{ subject to } x \in \mathbb{R}^n, \|Ax - b\|_2 \leq \eta \quad (3)$$

is unique, then  $x^\#$  is  $\text{rk}(A)$ -sparse, where  $\text{rk}(A)$  denotes the rank of  $A$ .

*Remark 1:*  $A \in \mathbb{R}^{m \times n}$  is fundamental in Theorem 1, which fails if  $A \in \mathbb{C}^{m \times n}$ . For this reason, when working on  $\mathbb{C}^d$ , we consider its structure as the real vector space  $\mathbb{R}^{2d}$ .

LASSO has many equivalent formulations, where the equivalence notion is specified in [3, Proposition 3.2]. We limit ourselves to delineate the relationship between the constrained LASSO (3) and its unconstrained counterpart:

$$\text{minimize} \quad \frac{1}{2}\|x\|_1 + \frac{\lambda}{2}\|Ax - b\|_2^2. \quad (4)$$

*Theorem 2:* Let  $A \in \mathbb{R}^{m \times n}$ ,  $b \in \mathbb{R}^m$  and  $\eta > 0$ . Let  $x^\#$  be a minimizer of the constrained LASSO (3). Then, there exists  $\lambda' \geq 0$  such that  $x^\#$  is also a minimizer of (4) with  $\lambda = \lambda'$ . Conversely, if  $x^\#$  is a minimizer of (4), there exists  $\eta' \geq 0$  such that  $x^\#$  is also a minimizer of (3) with  $\eta = \eta'$ .

Consequently, solving (4) with the corresponding Lagrange multiplier provides a  $\text{rk}(A)$ -sparse solution. Theorem 2 holds also for g-LASSO:

$$\text{minimize} \quad \frac{1}{2}\|Ax - b\|_2^2 + \frac{\lambda}{2}\|\Phi x\|_1, \quad (5)$$

the rescaling by the factor  $1/2$  is needed for computational purposes, but it is irrelevant to the analysis of (5). Also, observe that (5) with  $\lambda \neq 0$  is equivalent to:

$$\text{minimize} \quad \frac{1}{2}\|\Phi x\|_1 + \frac{\lambda}{2}\|Ax - b\|_2^2, \quad (6)$$

where the equivalence follows by choosing  $\lambda^* = \lambda^{-1}$ .

### B. Construction of Lagrange multipliers

The construction of a Lagrange multiplier is detailed in the proof of [12, Theorem 4.8], which uses Hahn-Banach theorem to find a hyperplane that separates two convex sets, which for (6) read as: the epigraph  $\mathcal{A} = \left\{ (u, t) \in \mathbb{R}^2 : u \geq \frac{1}{2}\|Ax - b\|_2^2 - \frac{\eta^2}{2}, t \geq \frac{1}{2}\|\Phi x\|_1 \text{ for some } x \in \mathbb{R}^n \right\}$  and the lower half-line  $\mathcal{B} = \left\{ (0, t) \in \mathbb{R}^2 : t < p^* \right\}$ , where  $p^* = \min\{\|\Phi x\|_1 : \|Ax - b\|_2 \leq \eta\}$  (see fig. 2).

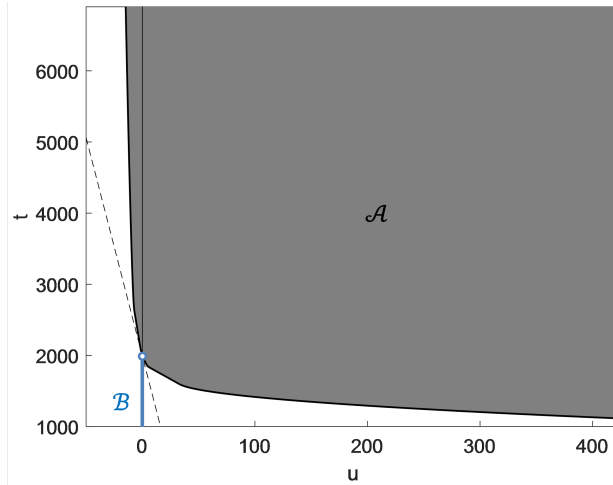


Fig. 2: A graphic representation of the sets  $\mathcal{A}$  and  $\mathcal{B}$ , and the separating hyperplane (dashed line). Observe that  $\mathcal{A}$  is an epigraph and  $\mathcal{B}$  is an open lower half-line. The closure of  $\mathcal{B}$  intersects the boundary of  $\mathcal{A}$ .

In the particular case of g-LASSO, separating hyperplanes are lines, and if  $t = mu + q$  is any separating line, then a Lagrange multiplier can be chosen as  $\lambda^* = -m$  or, equivalently,  $\lambda = -1/m$ . Let us observe that set  $\mathcal{B}$  serves no essential purpose in determining a separating line, as it merely constitutes a lower half-line intersecting  $\mathcal{A}$  at its boundary. Additionally, when the lower boundary of  $\mathcal{A}$  is  $\mathcal{C}^1$  regular in a neighborhood of  $u = 0$ , a numerical approach enables the identification of a separating line by delineating  $\mathcal{A}$  and computing the tangent at 0 along the graph of its boundary.

### C. Main challenges

A direct application of the theory described so far for deriving tuning parameters poses three main challenges.

- **Necessity of numerical methods:** in the vast majority of convex optimization problems, the expression of the dependence  $\lambda = \lambda(x^\#)$  or even  $\lambda = \lambda(\eta)$ , is a challenging task. We refer to [13] for examples of weighted LASSO problems where this relation is instead explicit. Hence, finding a Lagrange multiplier with the construction in [12] requires a separating line to be found numerically.
- **Unknown constraints:** theoretically, the numerical machinery described above necessitates prior knowledge of  $\eta = \|Ax^\# - b\|_2$ , where  $x^\#$  is the solution of g-LASSO. Consequently, the cylinder  $\Gamma_\eta = \{x : \|Ax - b\|_2 \leq \eta\}$  is not only unknown, but it depends heavily on the outcome of g-LASSO.
- **Dimensionality:** outlining  $\mathcal{A}$  or its boundary necessitates plotting  $\infty^n$  points in  $\mathbb{R}^2$ , rendering it an impractical endeavor.

While acknowledging the necessity of numerical analysis, we may resort to an escamotage to overcome the two remaining challenges. However, this entails abandoning the pursuit of exact Lagrange multipliers in favor of approximations. The constraint bound  $\eta$  depends intrinsically on the solution  $x^\#$  of g-LASSO, which in general differs from the ground truth  $f$  which, in the case of our experimental setting, consists of the Shepp-Logan phantom (see fig. 5 (A)).

Defining a constrained bound  $\eta$  induces a solution  $x^\#$  and reversely, a given solution  $x^\#$  sets the constraint bound  $\eta$ . In practice the solution  $x^\#$  is of course unknown and it is a subtle task to choose  $\eta$  appropriately so that the solution  $x^\#$  is, hopefully, as close as possible to the ground truth. Choosing  $\eta$  is equivalent to choosing the allowed amount of error on the raw data. It follows that  $\eta$  must be at least as large as the noise amplitude. Other sources of error can also add to the noise so that in general  $\eta$  may be larger than the noise amplitude. This being said, in the present study, we chose to set  $\eta$  to be equal to the norm of the added noise

$$\eta = \|Af - b\|_2 = \|\varepsilon\|_2.$$

This situation is still far from concrete, since  $\|\varepsilon\|_2$  is not known in the practice. However, we note that the purpose of the present study is to present an ideal situation to test if it is possible to use approximations of Lagrange multipliers as well-performing tuning parameters for generalized LASSO problems, shifting the focus from selecting the tuning parameter to estimating the noise energy.

Consequently, the tuning parameter returned by ALMA serves as an *approximate Lagrange multiplier*, rather than the exact one. Achieving this approximation involves outlining the corresponding epigraph  $\mathcal{A}$ . The essence of ALMA lies in a technicality allowing for the approximation of  $\mathcal{A}$  by sketching infinitely many of its points simultaneously, as outlined below.

### D. The MRI model

For the sake of concreteness, we simulate the reconstruction of a MR signal. Let us spend a few words about how g-LASSO is used, and why the correct choice of  $\lambda$  is fundamental, in the context of MRI. Roughly speaking, the (inverse) spatial Fourier transform of the MR signal is the anatomical image of a tissue, which is supported in a cube  $[-L_x/2, L_x/2] \times [-L_y/2, L_y/2] \times [-L_z/2, L_z/2]$ . By Shannon's theorem full Cartesian (uniform) sampling consists of sampling  $n_x$  points in the  $k_x$  direction,  $n_y$  points along the  $k_y$  direction and  $n_z$  points along the  $k_z$  direction of the k-space, where:

$$\Delta x = \frac{L_x}{n_x}, \quad \Delta y = \frac{L_y}{n_y}, \quad \Delta z = \frac{L_z}{n_z},$$

and

$$\Delta k_x = \frac{1}{L_x}, \quad \Delta k_y = \frac{1}{L_y}, \quad \Delta k_z = \frac{1}{L_z},$$

we mention [1] as reference therein.

For various reasons, sampling the MRI signal at its Nyquist frequency poses several challenges, necessitating techniques that can accurately reconstruct the MRI signal from samples taken below the Nyquist frequency. First, in our 2D experiments the dimensionality of the problem is of the order of  $n = n_x n_y = 384^2 \sim 10^5$ . For a 3D image, it increases to  $n = n_x n_y n_z \sim 10^8$ , making the processing of the MRI signal extremely time-consuming and computationally expensive. Secondly, MRI requires patients to remain still throughout the entire acquisition process, making it challenging to image moving organs and to perform scans on patients with conditions such as movement disorders. Furthermore, MRI is extremely expensive, and reducing the amount of information to be acquired can lead to significant cost savings.

In light of these reasons, CS offers a valuable solution for reducing both acquisition time and computational costs. However, there are situations where CS transcends being merely advantageous: it becomes imperative. Take, for example, 3D-CINE MRI, where sampling a full-Cartesian grid would be excessively time-consuming to the extent that achieving full sampling becomes practically infeasible. The application of CS to MRI is called CS-MRI. Since the MR signal is known to be sparse with respect to the DFT, DWT, and other sparsity promoting transforms, cf. [2], g-LASSO is used for the purpose. In this

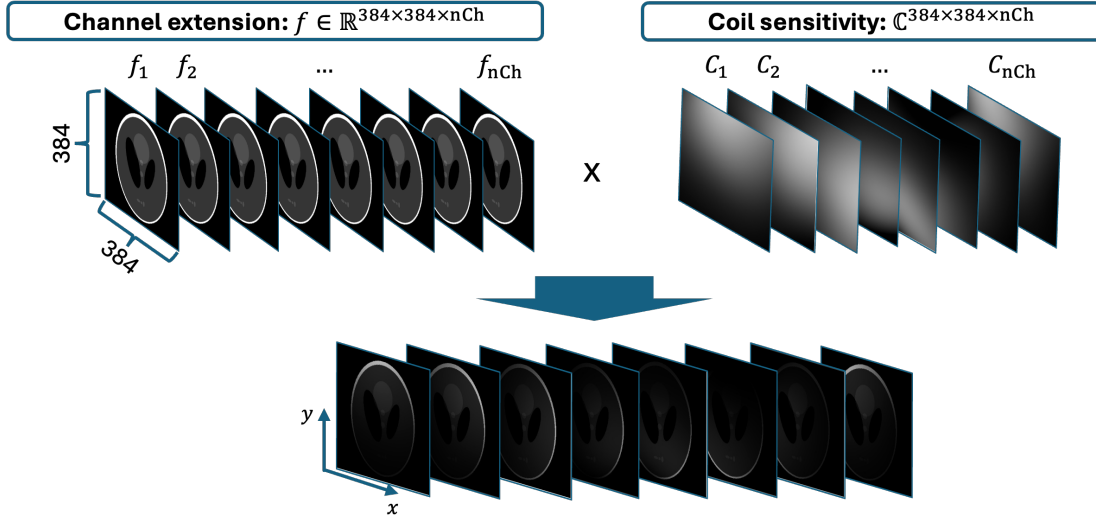


Fig. 3: Simulated channel extension and acquisition across coils.

work, we use the Shepp-Logan phantom and corrupt the data with artificial noise. The Shepp-Logan phantom is piecewise constant and, therefore, its gradient is sparse. For this reason, we use the discrete gradient as sparsity promoting transform:

$$D = \begin{pmatrix} -1 & 1 & 0 & \dots & 0 & 0 \\ 0 & -1 & 1 & \dots & 0 & 0 \\ \vdots & \vdots & \vdots & \ddots & \vdots & \vdots \\ 0 & 0 & 0 & \dots & -1 & 1 \end{pmatrix}, \quad (7)$$

and we set  $TV(x) = \|Dx\|_1$  (discrete anisotropic spatial total variation).

### III. EXPERIMENTAL DESIGN

The experiments were conducted using MATLAB\_R2023b. The Monalisa toolbox was used for MRI reconstructions.

#### A. The simulated MR signal

To simulate the acquisition of an MR signal, we considered the Shepp-Logan brain phantom  $f \in \mathbb{R}^{384 \times 384}$ , simulate coil sensitivity, undersampling, and Gaussian noise. MR data is sampled by a certain number  $nCh$  of coils simultaneously (parallel imaging). Let us delve into a detailed exposition of the data simulation, briefly summarized in the previous lines.

- 1) **Channel extension and acquisition across coils:**  $f$  is replicated  $nCh = 8$  times and each replica  $f_j \in \mathbb{R}^{384 \times 384}$ ,  $j = 1, \dots, nCh$ , is pointwise multiplied by a simulated coil sensitivity matrix  $C_j \in \mathbb{C}^{384 \times 384}$ :

$$f_k(i, j) = C_k(i, j)f(i, j),$$

$k = 1, \dots, nCh$ ,  $i, j = 1, \dots, 384$  (fig. 3).

- 2) **Fourier transform:** the spatial discrete Fourier transform of each  $f_j$  is computed (see fig. 9B).
- 3) **Undersampling:** full Cartesian sampling consists of sampling  $nLines = 384$  lines evenly spaced, whereas undersampling entails sampling only a certain fraction of these 384 lines, which we denote by  $UR\%$ . In our study, we tested undersampling rates of 10%, 15% and 20%, that is  $UR\% \in \{10/100, 15/100, 20/100\}$ . For a fixed  $UR\%$ , the sampling trajectory comprises  $n(UR\%) = \lceil nLines \cdot UR\% \rceil$  lines. The 30% of the  $n(UR\%)$  lines are used to sample the center of the k-space at the Nyquist frequency. Specifically,  $\lceil n(UR\%) \cdot 30/100 \rceil$  lines sample the center of the k-space, while the remaining lines sample the periphery of the k-space following a normal distribution  $\mathcal{N}(\mu, \sigma^2)$  with  $\mu = nLines/2 + 1$  and  $\sigma^2 = nLines \cdot UR\%$  (see fig. 9C). The Fourier transform of each coil-image is sampled according to the Cartesian undersampled trajectory established before. Consequently, the resulting simulated MR data consists of a tensor  $y \in Y = \mathbb{C}^{(nLines \cdot n(UR\%)) \times nCh}$  (see fig. 9D).
- 4) **Noise corruption:** we tested ALMA under three distinct noise levels. Specifically, the simulated MR data is given by:  $b = y + \varepsilon$ , where  $\varepsilon \in Y$  and  $\Re(\varepsilon_{i,j}), \Im(\varepsilon_{i,j}) \sim \mathcal{N}(0, \sigma^2)$  ( $i = 1, \dots, nLines \cdot n(UR\%)$  and  $j = 1, \dots, nCh$ ). We refer to  $\sigma^2$  as to noise level, which is computed as  $\sigma^2 = \|y\| \cdot NL\%$ , where in our experiments  $NL\% \in \{3/100, 5/100, 7/100\}$ . For instance, the terminology 3% noise means that we are considering  $NL\% = 3/100$ .

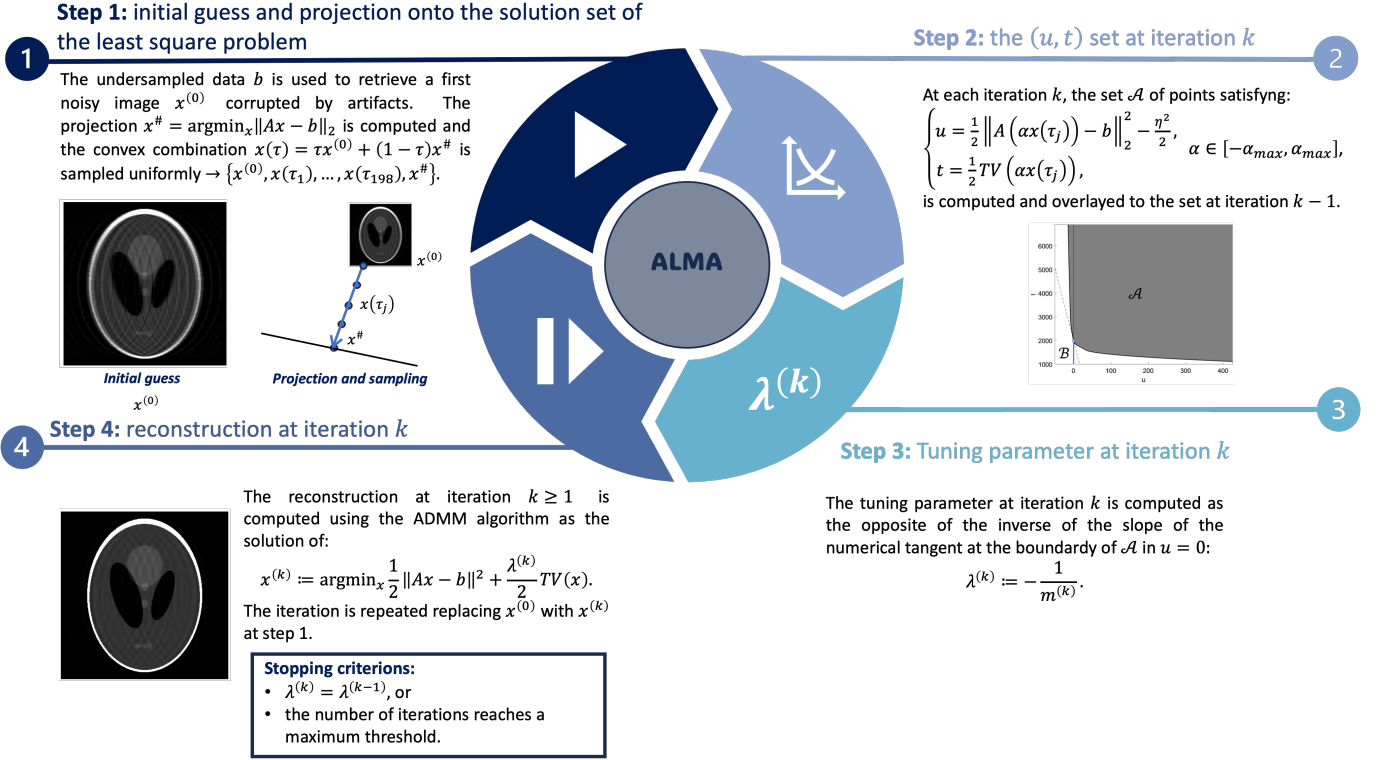


Fig. 4: Schematic representation of ALMA.

## B. ALMA

ALMA is synthesised in fig. 4 and schematized in Algorithm 1, here we limit to comment how ALMA computes a ALM. Note that the scalar product  $a^T b$ ,  $a, b \in \mathbb{R}^n$ , must be replaced with  $Re(a^T b)$  when  $a, b \in \mathbb{C}^n$ , where  $Re$  denotes the *real part*. Moreover, for non-Cartesian MRI trajectories, the scalar product that shall be considered is  $\langle a, b \rangle = Re(a^T H b)$ , with  $H$  Hermitian positive-definite matrix encoding the non-Cartesian gridding of the k-space.

In the previous paragraphs we observed that finding an ALM is a matter of tracing the tangent line in 0 to the epigraph  $\mathcal{A} = \{(u, t) \in \mathbb{R}^2 : u \geq \|Ax - b\|_2^2 / 2 - \eta^2 / 2, t \geq TV(x) / 2 \text{ for some } x \in \mathbb{R}^n\}$ , where  $\eta = \|A f - b\|_2$ , being  $f \in \mathbb{R}^{384 \times 384}$  the  $384 \times 384$  Shepp-Logan phantom. We pointed out that outlining  $\mathcal{A}$  is technically difficult due to the unfeasible dimensionality: in principle, for every  $x \in \mathbb{R}^n$  ( $n = 384^2$ ), once the point  $(u, t) = (u(x), t(x)) = 1/2 \cdot (\|Ax - b\|_2^2 - \eta^2, TV(x))$  is computed, one has that all the points of the first quadrant centered in  $(u(x), t(x))$  belong to  $\mathcal{A}$ . Clearly, it would be enough to compute  $(u(x), t(x))$  only for  $x \in \mathbb{R}^n$  such that  $(u(x), t(x))$  belongs to the boundary  $\partial \mathcal{A}$  of  $\mathcal{A}$ , but we do not have access to those points. On top of that, computing  $(u(x), t(x))$  for a fixed  $x$  is computationally expensive, because of the measurement operator  $A$ . However, a meaningful family of points  $(u(x), t(x))$  that would be enough to approximate the tangent line in 0 to its boundary can be found as follows:

- 1) Choose  $x \in \mathbb{R}^n$  so that the corresponding  $(u(x), t(x))$  is as far to the left of  $\mathcal{A}$  as possible. Clearly, this task is accomplished by any minimizer of  $\phi(x) = \|Ax - b\|_2^2$ , which consists of iterative SENSE reconstructions. Let us call this point  $x^\#$ .
- 2) Choose another point, for instance, the reconstructed image obtained by the gridded reconstruction of the noisy undersampled data,  $b$ . Let us call this point  $x^{(0)}$ .
- 3) Consider the segment that joins  $x^\#$  to  $x^{(0)}$  in the image domain and sample it at a rate decided a priori, e.g. 201 uniformly spaced samples.
- 4) Let  $x$  be one of this samples. Compute  $\|Ax\|_2^2$ ,  $b^T Ax$  and  $TV(x)$ .
- 5) The curve  $\gamma_x$  parametrized by  $\alpha \in \mathbb{R}$  as:

$$\begin{aligned} \gamma_x(\alpha) &= (u(\alpha x), t(\alpha x)) \\ &= \frac{1}{2} (\alpha \|Ax\|_2^2 - 2\alpha b^T Ax + \|b\|_2^2 - \eta^2, \alpha |TV(x)|) \end{aligned}$$

consists of a couple of branches of parabolas. The parameters  $\alpha_1$  and  $\alpha_2$  such that  $\gamma_x(\alpha_1)$  and  $\gamma_x(\alpha_2)$  are the vertices of these parabolas can be computed explicitly by the expression of  $\gamma_x(\alpha)$ .

---

**Algorithm 1** ALMA
 

---

**Require:** : maximal number of iterations:  $n_{max}$ .

**Require:** :  $A \in \mathbb{C}^{m \times n}$  and  $b \in \mathbb{C}^m$ .

**Require:** :  $x^\#$  ground-truth and set  $\eta = \|Ax^\# - b\|_2$ .

**Require:** :  $x^{(0)} = \arg \min_{x \in \mathbb{C}^n} \|Ax - b\|_2$ .

**while**  $n \leq n_{max}$  **do**

1. Project  $x^{(n-1)}$  onto the solution set of the least-square problem, call  $x_{proj}^{(n-1)}$  the projection.
2. Consider the convex combination  $x_\tau^{(n)} = \tau x^{(n-1)} + (1 - \tau)x_{proj}^{(n-1)}$  ( $0 \leq \tau \leq 1$ ).
3. Consider a partition  $\tau_1 = 0, \dots, \tau_{200} = 1$  of  $[0, 1]$  and the related  $x_{\tau_j}^{(n)}$ .

**while**  $1 \leq j \leq 200$  **do** Plot the set  $\mathcal{A}$  of points  $(u, t) \in \mathbb{C}^2$  in the form

$$\begin{cases} u = \frac{1}{2} \|A(\alpha_k x_{\tau_j}^{(n)}) - b\|_2^2 - \frac{\eta^2}{2}, \\ t = \frac{1}{2} TV(\alpha_k x_{\tau_j}^{(n)}), \end{cases}$$

where  $\alpha_k \in [-\alpha_{max}, \alpha_{max}]$  is an equally spaced sequence ( $k = 1, \dots, k_{max}$ ),

$$\alpha_{max} = \frac{|b^T A x_{\tau_j}^{(n)}|}{\|A x_{\tau_j}^{(n)}\|_2^2}.$$

**end while**

4. Compute the slope  $m^{(n)}$  of the tangent to the lower boundary of  $\mathcal{A}$ , in  $u = 0$ . Set  $\lambda^{(n)} = -1/m^{(n)}$ .
5. Solve

$$\arg \min_{x \in \mathbb{C}^n} \frac{1}{2} \|Ax - b\|_2^2 + \frac{\lambda^{(n)}}{2} TV(x)$$

with the ADMM algorithm. Call  $x^{(n)}$  the solution.

**if**  $n > 1$  and  $\lambda^{(n)} = \lambda^{(n-1)}$  **then** Break

**end if**

**end while**

**Result:**  $x_{out} = x^{(r)}$ , where  $r$  is the number of iterations at the end of **while**.

---

- 6) Let  $\alpha_{max} = \max\{|\alpha_1|, |\alpha_2|\}$ . Compute and plot  $\gamma_x(\alpha)$  for  $\alpha \in [-\alpha_{max}, \alpha_{max}]$ . Since  $\|Ax\|_2^2$ ,  $b^T Ax$  and  $TV(x)$  have been computed in 4., the computational cost of this operation is low.
- 7) Repeat the procedure for every  $x$  belonging to the segment that joins  $x^\#$  to  $x^{(0)}$ .
- 8) Since  $\mathcal{A}$  is known to be convex, compute the convex hull of the outlined points.

The convex hull at the end of 8. is the approximation of  $\mathcal{A}$  at iteration 1.

- 9) Choose  $\lambda^{(1)} = -1/m^{(1)}$ , where  $m^{(1)}$  is the slope of the tangent and reconstruct an image using  $\lambda^{(1)}$  as tuning parameter for TV-LASSO. Call this image  $x^{(1)}$ .

Indicatively,  $x^{(1)}$  has the advantage of being more regular than  $x^{(0)}$ , that is  $TV(x^{(1)}) \leq TV(x^{(0)})$ .

- 10) Repeat steps 1)-9) replacing  $x^{(0)}$  with  $x^{(1)}$ , to outline points of  $\mathcal{A}$  that are narrower with respect to the points outlined in steps 1)-7). Overlaying these new points to the ones already outlined in 7), improves the approximation of  $\mathcal{A}$ .
- 11) Compute the slope  $m^{(2)}$  of the new tangent in 0 to the convex boundary of  $\mathcal{A}$  and define  $\lambda^{(2)} = -1/m^{(2)}$ .

### C. Image quality metrics

We measured quantitatively the quality of the output of ALMA by means of three metrics: the mSSIM, the pSNR and the CJV.

- The mSSIM is an extension of the structural similarity index, designed to assess the quality of reconstructions across various scales in a manner that approximates human perception, c.f. [14], [15]. It compares the brightness, contrast, and structural details of reconstructions with ground truth images, assigning values on a scale from 0 to 1, where a score of 1 indicates optimal similarity. Good quality reconstructions typically correspond to mSSIM values of  $\geq 0.9$ . In the present work, the mSSIM is computed via the command `multissim(I, Iref)`, where `Iref` is the reference image (the Shepp-Logan brain phantom) and `I` is the image to be assessed.
- The pSNR quantifies noise corruption of compressed images, independently on the quality as perceived by human vision and good visual quality requires pSNR to be at least 30dB, c.f. [16].

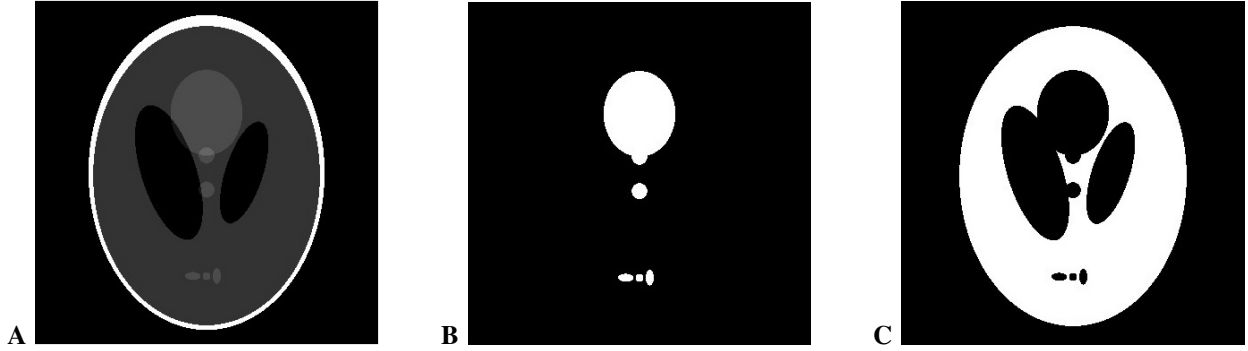


Fig. 5: The Shepp-Logan brain phantom (A). Grey matter (B) and white matter (C) masks for CJV computation.

- CJV measures the presence of intensity non-uniformity (INU) artifacts in MRI, c.f. [17], [18]. In the current paper, we use it as a measure of artifact bias in reconstructions. Lower values of CJV indicate better quality of MR images in terms of artifacts. CJV is defined based on the intensity difference between grey and white matter. Fig. 5 illustrates the masks corresponding to grey matter (B) and white matter (C) in the Shepp-Logan phantom, used for the computation of the CJV, as inspired by [19].

The notation  $mSSIM(\lambda)$  stands for the mSSIM of the reconstruction obtained by solving:

$$\arg \min_{x \in \mathbb{C}^n} \frac{1}{2} \|Ax - b\|_2^2 + \frac{\lambda}{2} TV(x). \quad (8)$$

Analogous notations for  $pSNR(\lambda)$  and  $CJV(\lambda)$ . The mSSIM takes values in  $[0, 1]$  and optimality corresponds to  $mSSIM(\lambda) = 1$  (maximum). The pSNR and the CJV take values in  $[0, +\infty)$  and are optimized in correspondence of their maxima and their minima respectively. Good quality with respect to mSSIM corresponds to  $mSSIM \geq 0.9$ , good quality with respect to pSNR corresponds to  $pSNR \geq 30\text{dB}$ . Assessing good quality for CJV is harder, since, differently from the mSSIM and the pSNR, the CJV is optimized in correspondence of its minima  $\arg \min(CJV(\lambda))$ , whereas  $\max(CJV(\lambda))$  potentially grows to infinity. For these reasons, we considered good quality with respect to CJV as:

$$\begin{aligned} CJV(\lambda) &\leq \min(CJV) + \frac{\max(CJV) - \min(CJV)}{10} \\ &= 0.0493 \approx 0.05, \end{aligned} \quad (9)$$

where  $\max(CJV) = \max\{CJV(\lambda) : 0 \leq \lambda \leq 2\}$  and  $\min(CJV) = \min\{CJV(\lambda) : \lambda \geq 0\}$ , analogous notations are used for the minima and the maxima of mSSIM and pSNR.

#### D. Data analysis

The mSSIM, pSNR, and CJV, along with their respective relative versions, serve as quantitative measures for assessing the quality of reconstructions. Additionally, the (unique, in our experiments) tuning parameters  $\lambda_{mSSIM}$ ,  $\lambda_{pSNR}$  and  $\lambda_{CJV}$  which optimize each metric can be considered. Specifically,  $\lambda_{mSSIM} = \arg \max\{mSSIM(\lambda) : \lambda \geq 0\}$ ,  $\lambda_{pSNR} = \arg \max\{pSNR(\lambda) : \lambda \geq 0\}$  and  $\lambda_{CJV} = \arg \min\{CJV(\lambda) : \lambda \geq 0\}$ . The ratios  $\lambda_{mSSIM}/\lambda_{ALM}$ ,  $\lambda_{pSNR}/\lambda_{ALM}$  and  $\lambda_{CJV}/\lambda_{ALM}$  express the distance between optimal tuning parameters (with respect to the metrics) and ALMs in terms of the orders of magnitude of the corresponding ratios. We term the ratio  $\lambda_{mSSIM}/\lambda$  the magnitude ratio corresponding to  $\lambda$  (with respect to mSSIM), and similar notations are reserved for the other metrics. For every pair  $(UR\%, NL\%)$  and every reconstruction, we calculate the mSSIM, pSNR and CJV, alongside their corresponding magnitude ratios. Within each fixed pair  $(UR\%, NL\%)$ , we employ violin plots to illustrate the distributions of mSSIM, pSNR and CJV across the 50 runs, for analysis. Additionally, shaded error bars for the functions  $mSSIM(\lambda/\lambda_{ALM})$ ,  $pSNR(\lambda/\lambda_{ALM})$  and  $CJV(\lambda/\lambda_{ALM})$  are incorporated to evaluate the optimality of ALMs as tuning parameters. A value of  $\lambda_{mSSIM}/\lambda_{ALM} = 1$  signifies that  $\lambda_{ALM}$  is the optimal tuning parameter with respect to mSSIM. Similar interpretations apply for the other magnitude ratios. For a comparison, we compute the L-curve tuning parameter  $\lambda_L$ , and execute reconstructions using TV-LASSO with this parameter. Subsequently, we compute  $mSSIM(\lambda_L)$ ,  $pSNR(\lambda_L)$  and  $CJV(\lambda_L)$ , along with the corresponding magnitude ratios pertaining to  $\lambda_L$  with respect to these three metrics.

#### E. The dataset

The dataset is obtained reconstructing an image for a fixed pair  $(UR\%, NL\%)$  50 times (number of runs), to ensure statistical robustness with respect to the sampling randomisation. The dataset consists of  $3 \times 3 \times 50$  reconstructions.

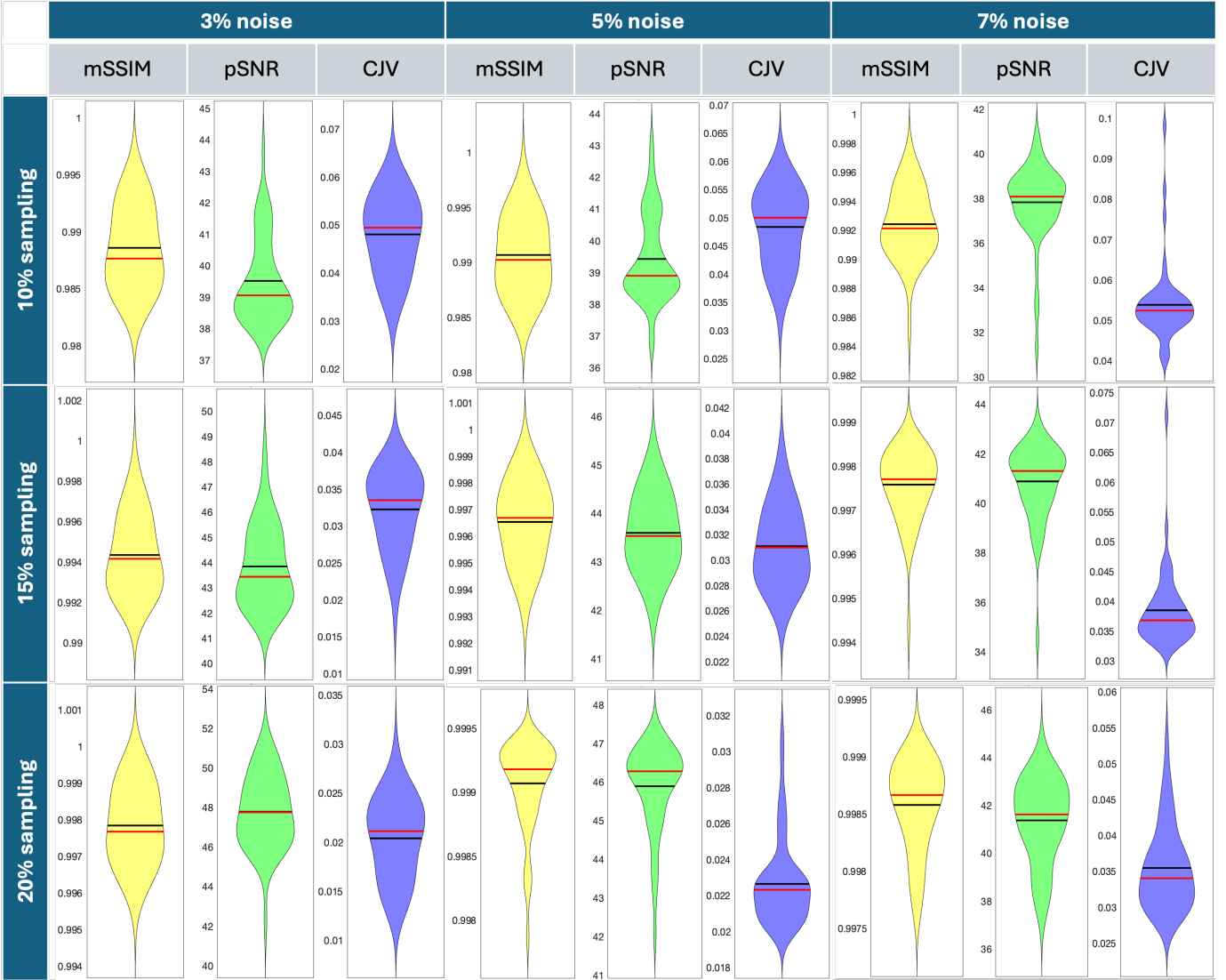


Fig. 6: Violin plots of the three metrics across noise levels and undersampling rates. Yellow violins correspond to mSSIM, green violins correspond to pSNR and purple violins correspond to CJV. The black lines correspond to the means and the red lines correspond to the medians.

## IV. RESULTS

### A. Analysis of convergence

For fixed noise level and undersampling rate, ALMA approximates an ALM by conducting reconstructions, updating the ALM approximation at each iteration. We have selected two stopping criteria:

- The number of iterations  $k$  reaches a predefined maximum (set to  $k_{max} = 100$ ).
- At iteration  $k_0 + 1$ ,  $\lambda^{(k_0+1)} = \lambda^{(k_0)}$ , in which case  $\lambda^{(k)} = \lambda^{(k_0)}$  for every  $k \geq k_0$ .

Note that the second criterion serves as a convergence criterion for ALMA. This means that if it is satisfied, ALMA not only stops but actually *converges* (i.e., the sequence  $(\lambda^{(k)})_k$  of ALMs at step  $k$  converges). Observe that in all of our experiments, the sequence of the ALMs is eventually constant. Therefore, in what follows, the term *convergence* will refer to ALMA stopping due to the fulfillment of the second stopping criterion.

Through empirical analysis, we investigated the convergence of ALMA across various noise levels and undersampling rates. As aforementioned, ALMA converges in a finite time for every undersampling rate and noise level.

The histograms in fig. 7 (A) illustrates the number of iterations required for the convergence of ALMA across different noise levels and undersampling rates. Both histograms follow Gaussian distributions that become less concentrated around 0 as the undersampling rate increases (fig. 7 (A)) or as the noise level rises (fig. 7 (B)). In both scenarios, the increase in the number of iterations can be attributed to the amount of information processed by ALMA, which grows with the number of sampling

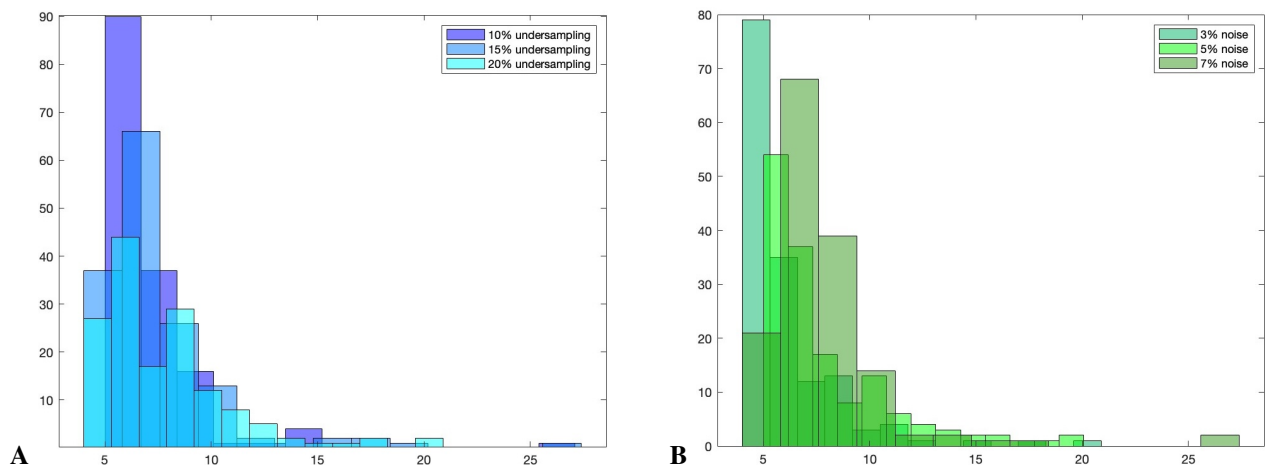


Fig. 7: Convergence analysis. Histograms of the number of iterations needed for ALMA’s convergence across undersampling rates (A) and noise levels (B). The number of bins for each histogram is the ceiling of the square root of the number of points, i.e.,  $\lceil \sqrt{150} \rceil = 13$ . Observe that the number of iterations for ALMA to stop is mostly concentrated in the interval  $[0, 10]$  independently of the noise level and the undersampling rate, while the standard deviations increase with the undersampling rate and the noise percentage. This demonstrates that the number of iterations required for ALMA to converge is relatively low even when processing larger amounts of information (20% undersampling) and higher noise percentages (7% noise).

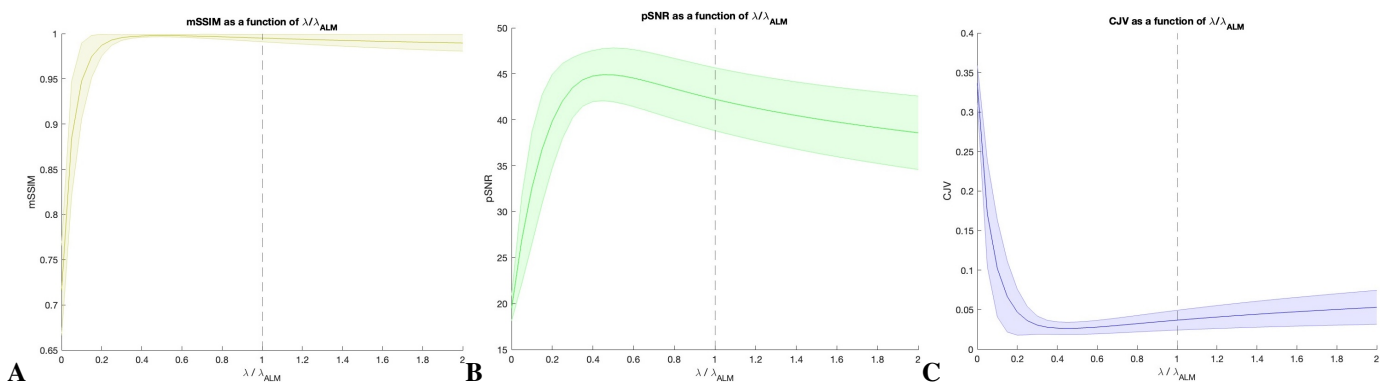


Fig. 8: Shaded error bar of the  $mSSIM$  (A),  $pSNR$  (B) and  $CJV$  (C) as functions of  $\lambda/\lambda_{ALM}$ , the shades representing the corresponding standard deviations. The values 1 on the horizontal axes correspond to  $\lambda = \lambda_{ALM}$ .

points and the noise level. Let us delve deeper into these cases. On average, ALMA stops after  $7.2089 \pm 2.9773$  iterations (see fig. 9). For the 10% sampling rate, both the average number of iterations and the standard deviation increase with the noise level. A similar trend is observed for the 15% undersampling rate, as detailed in fig. 9. However, the 20% sampling rate exhibits a distinct pattern: the average number of iterations increases from 3% to 5% noise levels and reaches its minimum at a noise level of 7%.

### B. Performance of ALMA with respect to $mSSIM$

Images reconstructed utilizing the ALMs computed by ALMA consistently exhibit an average  $mSSIM \geq 0.99$ , irrespective of the noise level or the undersampling rate (see fig. 9). The violin plots for the  $mSSIM$  are displayed in figure 6 (color yellow).

Across noise levels and undersampling rates, the tuning parameter that optimizes the  $mSSIM$  ( $\lambda_{mSSIM}$ ) is around half of the ALM ( $\lambda_{ALM}$ ), i.e.  $\lambda_{mSSIM} \approx 0.52 \cdot \lambda_{ALM}$  (see fig. 9). However, even if  $\lambda_{ALM}$  does not maximize the  $mSSIM$ , the points  $(1, mSSIM(1))$ , which correspond to the  $mSSIM$  of the reconstructions obtained with ALMs, always lie on the plateau of the graph of the function  $mSSIM(\lambda/\lambda_{ALM})$ , indicating that  $\lambda_{ALM}$  is in the range of tuning parameters corresponding to almost-optimal  $mSSIM$  values (see fig. 8 (A)).

### C. Performance of ALMA with respect to $pSNR$

Reconstructions obtained using ALMA exhibit high  $pSNR$  for every noise level and undersampling rate. As expected the  $pSNR$  decreases across noise levels. On average, the  $pSNR$  is  $\geq 40$ dB for reconstructions of images corresponding to 15%

		iterations	mSSIM	pSNR (dB)	CJV	$\lambda_{mSSIM}/\lambda_{ALM}$	$\lambda_{pSNR}/\lambda_{ALM}$	$\lambda_{CJV}/\lambda_{ALM}$
10% sampling	3% noise	5.3600 ± 0.6627	0.9886 ± 0.0036	39.5220 ± 1.3622	0.0481 ± 0.0078	0.2680 ± 0.0705	0.3680 ± 0.0705	0.3890 ± 0.0865
	5% noise	6.8000 ± 2.2497	0.9907 ± 0.0034	39.4282 ± 1.3789	0.0484 ± 0.0069	0.4610 ± 0.0680	0.4610 ± 0.0680	0.4930 ± 0.0572
	7% noise	8.1000 ± 3.3089	0.9924 ± 0.0024	37.8291 ± 1.7134	0.0538 ± 0.0095	0.4460 ± 0.0748	0.4460 ± 0.0748	0.4430 ± 0.0553
15% sampling	3% noise	5.4800 ± 1.4741	0.9943 ± 0.0019	43.8485 ± 1.5849	0.0323 ± 0.0053	0.4210 ± 0.0881	0.4210 ± 0.0881	0.3770 ± 0.0771
	5% noise	7.5600 ± 2.9496	0.9965 ± 0.0015	43.5978 ± 0.8036	0.0311 ± 0.0032	0.6190 ± 0.0832	0.6190 ± 0.0832	0.5510 ± 0.0576
	7% noise	8.7000 ± 3.4181	0.9976 ± 0.0008	40.8857 ± 1.4965	0.0385 ± 0.0063	0.4700 ± 0.0953	0.4700 ± 0.0953	0.4700 ± 0.0964
20% sampling	3% noise	7.6000 ± 3.2514	0.9978 ± 0.0011	47.7808 ± 1.8292	0.0204 ± 0.0041	0.5460 ± 0.0903	0.5460 ± 0.0903	0.5030 ± 0.0785
	5% noise	9.5600 ± 3.0650	0.9991 ± 0.0003	45.8925 ± 1.1229	0.0226 ± 0.0024	0.5290 ± 0.1306	0.5290 ± 0.1306	0.5080 ± 0.1144
	7% noise	5.7200 ± 1.6293	0.9986 ± 0.0004	41.3764 ± 1.7199	0.0355 ± 0.0058	0.3590 ± 0.0973	0.3590 ± 0.0973	0.3530 ± 0.0928
Averages and stds		7.2089 ± 2.9473	0.9951 ± 0.0041	42.2401 ± 3.4208	0.0367 ± 0.0125	0.4688 ± 0.1200	0.4688 ± 0.1200	0.4541 ± 0.1034

Fig. 9: Means and standard deviations of the number of iterations, the three metrics, and the magnitude ratios across undersampling rate and noise level, for the reconstructions obtained using the ALM. Observe that the average number of iterations is 7, and the three metrics exhibit average values of approximately 0.9951, 42.2401 dB, and 0.0367, respectively, indicating optimal performance of ALMA.

and 20% undersampling rates, whereas the average pSNR of reconstructions with 10% undersampling rate is at least 35dB (see fig. 9). Other than demonstrating the quality of reconstructions obtained via ALMA in terms of pSNR, this reflects the fact that solving TV-LASSO with ALMs as tuning parameters tend to produce highly regularized images. Again, across noise levels and undersampling rates, the tuning parameter that optimizes the pSNR ( $\lambda_{pSNR}$ ) tends to be approximately 0.47 times the corresponding ALM, i.e.  $\lambda_{pSNR} \approx 0.47 \cdot \lambda_{ALM}$  (see fig. 9). Compared to the graphs  $mSSIM(\lambda/\lambda_{ALM})$ , the plateau of the functions  $pSNR(\lambda/\lambda_{pSNR})$  near their maxima is less pronounced, and the points  $(1, pSNR(1))$ , corresponding to the pSNR of reconstructions obtained with ALMs, are shifted to the right of their peaks (see fig. 8 (B)). In conclusion, ALMs perform almost-optimally with respect to pSNR.

#### D. Performance of ALMA with respect to CJV

Except for the worst-case scenario  $UR\% = 10\%$ ,  $NL\% = 7\%$ , the reconstructions obtained by ALMA display CJV values no larger than 0.05, showing that ALMA performs well with respect to CJV as well (see fig. 9). The tuning parameter that minimizes the CJV ( $\lambda_{CJV}$ ) is on average 0.45 times the corresponding ALM, i.e.  $\lambda_{CJV} \approx 0.45 \cdot \lambda_{ALM}$  (see fig. 9). However, ALMs still perform almost optimally with respect to CJV, and the points  $(1, CJV(1))$ , corresponding to the CJV of reconstructions obtained with ALMs, are shifted to the right of their minima, in accordance with the behavior of the graphs  $pSNR(\lambda/\lambda_{CJV})$  (see fig. 8 (C)).

#### E. Comparison with the L-curve parameter

For a comparison, we report on the quantitative measurement regarding the reconstructions obtained utilizing the parameter  $\lambda_L$ , computed by L-curve. These reconstructions exhibit an average  $mSSIM \geq 0.99$ , across noise levels and undersampling rates (see fig. 11), they also exhibit an average pSNR of 42.6351 and an average CJV of 0.035. Therefore, they perform well regarding the metrics criterion. Moreover, the tuning parameter that minimizes the mSSIM ( $\lambda_{mSSIM}$ ) is on average 0.6 times the corresponding  $\lambda_L$ , i.e.  $\lambda_{mSSIM} \approx 0.6 \cdot \lambda_L$ , while the tuning parameters optimizing the pSNR and the CJV ( $\lambda_{pSNR}$  and  $\lambda_{CJV}$ , resp.) are on average 0.5 times  $\lambda_L$  (see fig. 11). All these data together show that the performance of the L-curve parameter is slightly better compared to the performance of the ALM. However, the difference is marginal and amounts to only a matter of decimals. Moreover, ALMA is an iterative procedure to compute tuning parameters and, consequently, solving TV-LASSO, whereas the L-curve method is heuristic and does not involve an iterative process. Despite yielding similar results, ALMA's iterative nature ensures a more robust and accurate determination of tuning parameters for solving TV-LASSO, offering a superior alternative to the heuristic approach of the L-curve method. Therefore, both methods perform similarly overall, indicating that the ALM is a reliable parameter, performing on par with the well-established L-curve method.

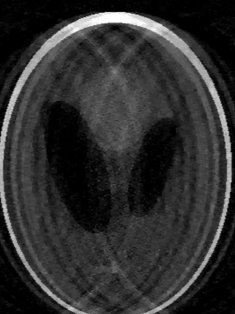
$\lambda = \lambda_{ALM}$	$\lambda = \lambda_L$	$\lambda = \lambda_{mSSIM} = \lambda_{pSNR}$	$\lambda = \lambda_{CJV}$
			
$mSSIM = 0.9882$ $pSNR = 38.3753$ $CJV = 0.0525$	$mSSIM = 0.9874$ $pSNR = 38.0796$ $CJV = 0.0544$	$mSSIM = 0.9964$ $pSNR = 41.5552$ $CJV = 0.0386$	$mSSIM = 0.9952$ $pSNR = 41.2745$ $CJV = 0.0375$
$\lambda = 0.0001$	$\lambda = 0.001$	$\lambda = 0.01$	$\lambda = 0.1$
			
$mSSIM = 0.7091$ $pSNR = 20.0032$ $CJV = 0.3037$	$mSSIM = 0.9422$ $pSNR = 29.4250$ $CJV = 0.1261$	$mSSIM = 0.9865$ $pSNR = 37.7847$ $CJV = 0.0554$	$mSSIM = 0.9038$ $pSNR = 23.1956$ $CJV = 0.2113$

Fig. 10: Example of reconstruction of simulated MRI data ( $NL_{\%} = 7/100$ ,  $UR_{\%} = 10/100$ ) with different tuning parameters: the ALM and the tuning parameter computed with the L-curve method, the tuning parameters that optimize each metric and tuning parameters that are powers of 10. The corresponding quantitative quality assessments are reported below each reconstruction. Observe that the quality of the reconstructions obtained using the ALM and the L-curve parameter are nearly indistinguishable, and close to the quality of the images reconstructed with the tuning parameters that optimize the metrics.

## V. DISCUSSION

We introduced ALMA for TV-LASSO, which demonstrated promising results in reconstructing undersampled and noisy MRI phantom data, achieving high-quality reconstructions without extensive manual tuning. We assessed the quality of the reconstructions quantitatively by means of mSSIM, pSNR and CJV.

As illustrated in fig. 10, the reconstruction quality using ALMA, even in the worst case scenario ( $UR_{\%} = 10\%$  and  $NL_{\%} = 7\%$ ), is notably superior when compared to parameter choices as powers of ten (see fig. 10). The reconstructed image via ALMA exhibits finer structural details and improved contrast, which are crucial for accurate diagnosis and analysis in clinical radiology.

To further validate ALMA's robustness, we compared its reconstructions to those obtained using parameters optimized for the three metrics (mSSIM, pSNR, and CJV). Figure 9 encapsulates this comparison, while fig. 10 provides a visual example of the reconstructions. The results indicate that ALMA's performance is nearly optimal, matching closely with the parameters that optimize each metric.

We also compared the performance of ALMA against the well-established L-curve method. As presented in fig. 9 and 11, and exemplified in fig. 10, both methods show comparable performance across the metrics. However, ALMA stands out as the first iterative algorithm to compute the parameter dynamically during reconstruction. This active, iterative approach grants ALMA significant advantages in computational efficiency and ease of implementation, which are particularly beneficial in clinical settings where a rapid and optimized reconstruction is essential.

Qualitatively, ALMA-reconstructed images maintain the anatomical integrity and structural fidelity necessary for clinical interpretation. This is evident in fig. 10, where even under severe noise and undersampling, the critical features are preserved.

		mSSIM	pSNR (dB)	CJV	$\lambda_{mSSIM}/\lambda_L$	$\lambda_{pSNR}/\lambda_L$	$\lambda_{CJV}/\lambda_L$
10% sampling	3% noise	$0.9881 \pm 0.0032$	$39.5421 \pm 1.0556$	$0.0484 \pm 0.0073$	$0.7348 \pm 0.2026$	$0.7494 \pm 0.2053$	$0.7947 \pm 0.2359$
	5% noise	$0.9911 \pm 0.0027$	$39.6677 \pm 1.1756$	$0.0440 \pm 0.0046$	$0.8564 \pm 0.0790$	$0.7768 \pm 0.0952$	$0.8351 \pm 0.1159$
	7% noise	$0.9923 \pm 0.0034$	$37.6640 \pm 2.3154$	$0.0555 \pm 0.0147$	$0.5962 \pm 0.2733$	$0.5241 \pm 0.2601$	$0.5112 \pm 0.2293$
15% sampling	3% noise	$0.9963 \pm 0.0016$	$44.2511 \pm 1.4122$	$0.0275 \pm 0.0042$	$0.3228 \pm 0.1609$	$0.3137 \pm 0.1512$	$0.2846 \pm 0.1555$
	5% noise	$0.9975 \pm 0.0010$	$43.7773 \pm 0.9432$	$0.0286 \pm 0.0026$	$0.5337 \pm 0.2205$	$0.5077 \pm 0.1786$	$0.4600 \pm 0.1785$
	7% noise	$0.9978 \pm 0.0006$	$40.9865 \pm 1.5365$	$0.0379 \pm 0.0053$	$0.5896 \pm 0.1991$	$0.4742 \pm 0.1392$	$0.4724 \pm 0.1309$
20% sampling	3% noise	$0.9988 \pm 0.0006$	$48.7886 \pm 1.1751$	$0.0170 \pm 0.0024$	$0.4246 \pm 0.0996$	$0.4022 \pm 0.0751$	$0.3723 \pm 0.0762$
	5% noise	$0.9992 \pm 0.0002$	$45.6172 \pm 1.3660$	$0.0228 \pm 0.0027$	$0.5787 \pm 0.2013$	$0.4753 \pm 0.1449$	$0.4580 \pm 0.1376$
	7% noise	$0.9989 \pm 0.0003$	$43.4215 \pm 1.4928$	$0.0301 \pm 0.0040$	$0.7700 \pm 0.2300$	$0.5675 \pm 0.1725$	$0.5579 \pm 0.1168$
Averages and stds		$0.9956 \pm 0.0043$	$42.6351 \pm 3.5832$	$0.0346 \pm 0.0135$	$0.6008 \pm 0.2493$	$0.5323 \pm 0.2174$	$0.5273 \pm 0.2372$

Fig. 11: Means and standard deviations of the number of iterations, the three metrics, and the magnitude ratios across undersampling rate and noise level, for the reconstructions obtained using  $\lambda_L$ , the tuning parameter of the L-curve.

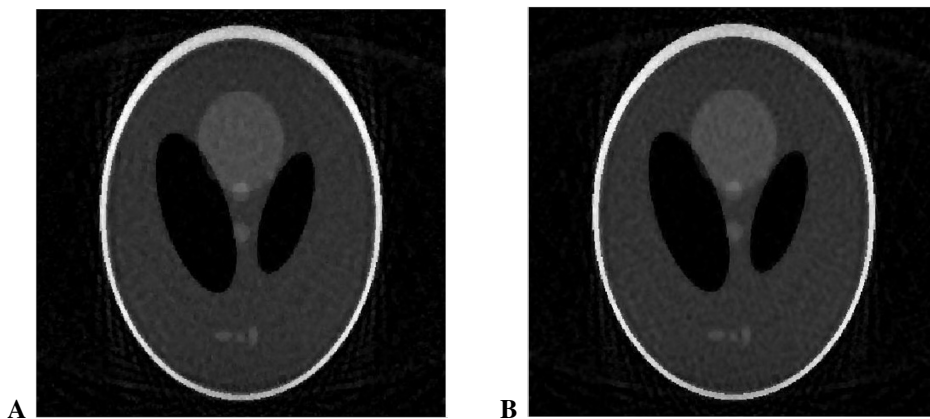


Fig. 12: Reconstructions of the Shepp-Logan brain phantom under radial sampling, with  $NL\% = 15/100$  and  $UR\% = 15\%$ . The reconstruction obtained with the ALM is displayed on the left. The reconstruction obtained with the parameter that maximizes the mSSIM is displayed on the right. Observe that the two images are almost indistinguishable.

Quantitatively, ALMA achieves high mSSIM, pSNR, and low CJV values, closely approximating the optimal values for these metrics obtained through extensive parameter optimization.

The strength of ALMA, however, does not limit to TV based LASSO denoising, or to Cartesian undersampling. For example, we repeated our experimental framework in extreme conditions ( $NL\% = 15/100$  and  $UR\% = 15\%$ ), but with radial sampling. The quality of the reconstruction is undoubtedly comparable to the best reconstruction in terms of mSSIM, as displayed in fig. 12.

## VI. CONCLUSIONS AND FUTURE DIRECTIONS

We achieved our three main objectives:

- We defined an iterative procedure to approximate Lagrange multipliers.
- We demonstrated the efficiency of ALMs as tuning parameters for TV-weighted g-LASSO in the context of MRI.
- We assessed the quality of the reconstructions using image quality metrics, including mSSIM, pSNR, and CJV.

Our results show that ALMA performs almost optimally across varying levels of noise and undersampling, consistently yielding high-quality reconstructions in terms of image quality metrics. This iterative algorithm offers significant advantages by actively computing the tuning parameter during reconstruction, which enhances computational efficiency and ease of implementation.

While our focus was on TV-LASSO, the principles underlying ALMA can be adapted to other models, paving the way for broader applications. For practical MRI applications, accurately estimating the norm of the noise remains a fundamental challenge for the implementation of ALMA. Such notwithstanding, our work serves as a basis, providing a solid foundation for future research aimed at improving parameter estimation and enhancing MRI reconstruction techniques.

## REFERENCES

- [1] D. W. McRobbie, E. A. Moore, M. J. Graves, and M. R. Prince, *MRI from Picture to Proton*. Cambridge university press, 2017.
- [2] M. Lustig, D. L. Donoho, J. M. Santos, and J. M. Pauly, "Compressed sensing mri," *IEEE signal processing magazine*, vol. 25, no. 2, pp. 72–82, 2008.
- [3] S. Foucart and H. Rauhut, *A Mathematical Introduction to Compressive Sensing*, 1st ed., ser. Applied and Numerical Harmonic Analysis. Birkhäuser New York, NY, 2013.
- [4] F. Santosa and W. W. Symes, "Linear inversion of band-limited reflection seismograms," *SIAM journal on scientific and statistical computing*, vol. 7, no. 4, pp. 1307–1330, 1986.
- [5] S. Chen and D. Donoho, "Basis pursuit," in *Proceedings of 1994 28th Asilomar Conference on Signals, Systems and Computers*, vol. 1. IEEE, 1994, pp. 41–44.
- [6] D. L. Donoho, "Compressed sensing," *IEEE Transactions on information theory*, vol. 52, no. 4, pp. 1289–1306, 2006.
- [7] R. Tibshirani, "Regression shrinkage and selection via the lasso," *Journal of the Royal Statistical Society Series B: Statistical Methodology*, vol. 58, no. 1, pp. 267–288, 1996.
- [8] M. Lustig, D. Donoho, and J. M. Pauly, "Sparse mri: The application of compressed sensing for rapid mr imaging," *Magnetic Resonance in Medicine: An Official Journal of the International Society for Magnetic Resonance in Medicine*, vol. 58, no. 6, pp. 1182–1195, 2007.
- [9] T. Çukur, M. Lustig, E. U. Saritas, and D. G. Nishimura, "Signal compensation and compressed sensing for magnetization-prepared mr angiography," *IEEE transactions on medical imaging*, vol. 30, no. 5, pp. 1017–1027, 2011.
- [10] S. S. Vasanawala, M. Murphy, M. T. Alley, P. Lai, K. Keutzer, J. M. Pauly, and M. Lustig, "Practical parallel imaging compressed sensing mri: Summary of two years of experience in accelerating body mri of pediatric patients," in *2011 IEEE International Symposium on Biomedical Imaging: From nano to macro*. IEEE, 2011, pp. 1039–1043.
- [11] S. S. Vasanawala, M. T. Alley, B. A. Hargreaves, R. A. Barth, J. M. Pauly, and M. Lustig, "Improved pediatric mr imaging with compressed sensing," *Radiology*, vol. 256, no. 2, pp. 607–616, 2010.
- [12] S. P. Boyd and L. Vandenberghe, *Convex optimization*. Cambridge university press, 2004.
- [13] G. Giacchi, B. Milani, and B. Franceschiello, "On the determination of lagrange multipliers for a weighted lasso problem using geometric and convex analysis techniques," *Applied Mathematics & Optimization*, vol. 89, no. 2, p. 31, 2024.
- [14] Z. Wang, E. P. Simoncelli, and A. C. Bovik, "Multiscale structural similarity for image quality assessment," in *The Thirty-Seventh Asilomar Conference on Signals, Systems & Computers, 2003*, vol. 2. Ieee, 2003, pp. 1398–1402.
- [15] L. Deligiannidis and H. R. Arabnia, *Emerging trends in image processing, computer vision and pattern recognition*. Morgan Kaufmann, 2014.
- [16] B. Adcock and A. C. Hansen, *Compressive imaging: structure, sampling, learning*. Cambridge University Press, 2021.
- [17] B. Likar, M. A. Viergever, and F. Pernus, "Retrospective correction of mr intensity inhomogeneity by information minimization," *IEEE transactions on medical imaging*, vol. 20, no. 12, pp. 1398–1410, 2001.
- [18] M. Ganzetti, N. Wenderoth, and D. Mantini, "Intensity inhomogeneity correction of structural mr images: a data-driven approach to define input algorithm parameters," *Frontiers in neuroinformatics*, vol. 10, p. 10, 2016.
- [19] R. Jaroudi, G. Baravdish, B. T. Johansson, and F. Åström, "Numerical reconstruction of brain tumours," *Inverse Problems in Science and Engineering*, vol. 27, no. 3, pp. 278–298, 2019.